8-2013

Transfer Impedance of Microperforated Materials with Tapered Holes

J Stuart Bolton
Purdue University, bolton@purdue.edu

Nicholas Kim
kim505@purdue.edu

Jonathan H. Alexander

Ronald W. Gerdes

T. Herdtle

Transfer impedance of microperforated materials with tapered holes

Thomas Herdtle

Predictive Engineering, 3M Company, St. Paul, Minnesota, 55144

J. Stuart Bolton

Nicholas N. Kim

Ray W. Herrick Laboratories, School of Mechanical Engineering, Purdue University, 140 S. Martin Jischke Drive, West Lafayette, Indiana 47907-2031

Jonathan H. Alexander

Automotive Division, 3M Company, St. Paul, Minnesota, 55144

Ronald W. Gerdes

Division Engineering, 3M Company, St. Paul, Minnesota, 55144

Running title (for bottom of page): **Tapered hole impedance**

Date uploaded to JASA system: 10/1/2012

ABSTRACT

It has been previously shown that relatively simple computational fluid dynamics (CFD) models can be used to calculate the transfer impedances, including the associated end corrections, of microperforated panels. The impedance is estimated by first calculating the pressure difference across a single hole when a transient input velocity is imposed, and then Fourier transforming the result to obtain the impedance as a function of frequency. Since the size of the hole and the dimensions of the inlet and outlet channels are very small compared to a wavelength, the flow through the hole can be modeled as incompressible. By using those procedures, Bolton and Kim extended Maa's classical theory to include a resistive end correction for sharp-edged cylindrical holes which differs from those previously proposed by the inclusion of a static component. Here it is shown that CFD models can also be used to compute end corrections for tapered holes. Since practical experimental characterization of perforated materials often involves measurement of the static flow resistance, a closed form empirical equation for that quantity has been developed. Finally, it is shown that configurations having equivalent static flow resistances can yield different acoustic absorptions.

PACS numbers: 43.55.Ev, 43.20.El

I. INTRODUCTION

The concept of microperforated absorbers was proposed by Maa more than thirty years ago and the related theory has been published in a number of different forms[1-3] (see Ref. 4 for a discussion of the various published forms of the Maa theory). Maa's theory combines Crandall's model for sound propagation in small diameter tubes[5] and Ingard's resistive end correction for perforations.[6] Both theoretical and experimental work has shown that microperforated absorbers can be effective over relatively broad frequency ranges and so they offer an attractive alternative to conventional sound absorbing materials, especially when the use of non-fibrous absorbers is desirable. Descriptions of potential applications in architectural acoustics and automotive noise control can be found in Refs. 7-9. Recently, there has also been interest in using microperforated lining materials in flow-duct noise control applications.[10-16] Further, microperforated materials may be incorporated into multi-layer systems to enhance particular aspects of the system performance.[17,18]

The theory of microperforated panels has also been extended to allow for the effect of panel flexibility. See, for example, Refs. 19-21 for a discussion of essentially infinite flexible permeable membranes, and Refs. 22-25 for a discussion of the effect of flexibility on finite microperforated systems at normal incidence, and Refs. 26-28 for more general incidence conditions. Less attention has been paid to the effect of hole shape (whether in plan shape or in the effect of variation of hole diameter with depth). In addition to cylindrical holes, slits have been studied[29], as have hourglass-shaped perforations[30] and tapered holes[31] (note that tapered holes of relatively large diameter are considered in Ref. 32: in that work, the holes are sufficiently large that viscous effects within the holes are

negligible, and so their behavior is quite different from microperforated materials). The study of tapered microperforations was the particular focus of the present work.

In the modeling domain, it has been shown that rigid perforated sheets may be modeled as rigid porous materials by an appropriate choice of macroscopic parameters.[33] That work also suggested that either rigid[16] or flexible[34] arbitrarily-shaped microperforated panels could be modeled using finite element methods. Recently, it has also been shown that the techniques of computational fluid dynamics (CFD) can be used to calculate the transfer impedance of rigid microperforated panels having cylindrical holes[35]. In that work, it was shown that the resistive end correction was essentially independent of frequency rather than depending on the square root of frequency as was previously suggested[6]. As a result, the conventional Maa theory results in an underestimate of the resistive end correction at low frequencies, as noted previously in Ref. 36.

Here the CFD procedure of Ref. 35 has been applied to the study of tapered microperforations. In particular, CFD was used to model the oscillatory, viscous flow though individual, sharp-edged, tapered holes. First, it is demonstrated for static flow how end effects for tapered holes can be incorporated into the usual Poiseuille term for the resistance. An analogous method is then applied to obtain an approximate, predictive formula for the dynamic flow resistance that reduces to the constant radius, cylindrical case in the appropriate limit. The CFD results clearly indicate, amongst other things, where the maximum energy dissipation occurs, and that the resistive end correction is associated with dissipation within the flow exterior to the hole rather than along the adjacent solid surface. Finally, it is demonstrated that the new formula allows the accurate prediction of normal incidence absorption of tapered hole, microperforated sheets positioned above a finite-

depth backing space.

II. REVIEW OF THEORY

The relevant equations for the present discussion are discussed in this section.

A. Maa Model

The Maa model can include both linear and non-linear components, the latter of which become significant only at high incident sound pressure levels[29]. In this study, the focus is on the linear part only, applicable for low to moderate sound pressure levels. The Maa model was derived for wave propagation in narrow tubes in which the oscillatory viscous boundary layer spans the hole diameter. For circular holes, the equation for the normal acoustic transfer impedance, Z, of a microperforated sheet with straight, constant-diameter holes, without end corrections, can be expressed as:

$$Z_{Maa} = \frac{j\rho\omega L}{\sigma}\left[1 - \frac{2}{k\sqrt{-j}}\frac{J_1\left(k\sqrt{-j}\right)}{J_0\left(k\sqrt{-j}\right)}\right]^{-1} \tag{1}$$

where ρ is the density of air, ω is the angular frequency, L is the length of the hole (or equivalently the thickness of the sheet), and σ is the porosity of the sheet (i.e., the fraction of the total surface area occupied by holes, which is equivalent to the fraction of the total sheet volume taken up by the holes). In addition, k is the perforation constant defined as:

$$k = d\sqrt{\rho\omega/(4\eta)} = r\sqrt{\rho\omega/\eta} \tag{2}$$

where η is the dynamic viscosity, d is the hole diameter, r is the hole radius (note that in this study either radius or diameter may be used, whichever best elucidates the relationships), and J_0 and J_1 are the Bessel functions of the first kind of zeroth and first order, respectively.

It should be noted, that in the limit of low frequencies, Eq. 1 can be approximated by:

$$Z_{Maa} \approx \frac{L}{\sigma}\left(\frac{8\eta}{r^2}+\frac{r^2\rho^2\omega^2}{144\eta}+\cdots\right)+j\frac{\rho\omega L}{\sigma}\left(\frac{4}{3}-\frac{r^4\rho^2\omega^2}{4320\eta^2}+\cdots\right). \quad (3)$$

The first term of the real part is the same result as that obtained from simple Poiseuille flow. Maa has presented the lowest order real and imaginary terms as an approximation of Eq. 1, but it is instructive to see the form of the first higher-order terms directly as functions of the frequency as well.

Additional energy dissipation occurs when the flow enters or exits a small hole. Maa used the concept of a surface resistance[6], defined by:

$$R_s = \sqrt{2\eta\rho\omega}\,/\,2 \quad (4)$$

to add resistive end effects to Eq. 1 above. He included a correction term to the reactance as well, derived from the radiation impedance of a piston, and together Maa's proposed end effects can written as:

$$Z_{Maa}^{End} = \frac{\rho}{\sigma}\left(\sqrt{\frac{\eta\omega}{2\rho}}+0.85jd\omega\right) \quad (5)$$

Note that both correction terms go to zero as the frequency goes to zero and therefore have no effect on the predicted static flow resistance.

B. Guo Model

Guo et al.[29] gave a modified form of Eq. 1 to account for hole geometry:

$$Z_{Guo} = \frac{j\rho\omega L}{\sigma}\left[1-\frac{2}{k\sqrt{-j}}\frac{J_1\left(k\sqrt{-j}\right)}{J_0\left(k\sqrt{-j}\right)}\right]^{-1}+\frac{\alpha 2R_s}{\sigma}+\frac{j\delta\rho\omega}{\sigma} \quad (6)$$

where α is a nominally frequency-independent factor which accounts for the hole type

(particularly sharp-edged or rounded); it was suggested that a value of 4 was appropriate for sharp-edged holes and 2 for rounded holes, whereas the form of Maa's resistive end correction implies a value of 0.5. The parameter δ is a factor for the mass end correction, sometimes known as the correction length, and Guo suggested a value of $\delta = 8d/3\pi$, matching that of Maa. Note that in the context of relatively large perforations, Ingard has shown that the end corrections are a function of perforation rate, with the corrections generally being reduced as the perforation rate increases. However, in the range of surface porosities usually considered appropriate for microperforated absorbers, this effect is negligible, and, as a result, surface porosity is not included as a parameter in the various formulae presented here. Therefore, the results of the present work strictly apply only to low surface porosity cases, and would need to be modified for cases in which the surface porosity was relatively large.

C. Bolton and Kim Model

Looking now just at the resistive part of the transfer impedance, Z_R, Bolton and Kim[35] found that for frequencies below about 5 kHz, the factor α in the real part of Guo's equation:

$$Z_R = \mathrm{Re}\left\{\frac{j\rho\omega L}{\sigma}\left[1 - \frac{2}{k\sqrt{-j}}\frac{J_1\left(k\sqrt{-j}\right)}{J_0\left(k\sqrt{-j}\right)}\right]^{-1}\right\} + \frac{\alpha\sqrt{2\eta\rho\omega}}{\sigma} \tag{7}$$

could better be represented as a function of frequency, instead of a constant. They found the functional form of a good approximation to be:

$$\alpha = \left(C_1\frac{L}{d} + C_2\right)\omega^{-0.5} \tag{8}$$

with C_1 and C_2 being constants. By substitution into Eq. 7,

$$Z_R = Re\left\{\frac{j\rho\omega L}{\sigma}\left[1-\frac{2}{k\sqrt{-j}}\frac{J_1(k\sqrt{-j})}{J_0(k\sqrt{-j})}\right]^{-1}\right\}+\frac{\sqrt{2\eta\rho}}{\sigma}\left(C_1\frac{L}{d}+C_2\right)\ . \quad (9)$$

In the latter form, it can be seen that the end correction proposed by Bolton and Kim is independent of frequency at low frequencies: i.e., there is a static, resistive end correction.

III. CFD MODEL

A. Geometry

To perform the CFD calculations, an axisymmetric model of a single tapered hole was created parametrically using general CFD codes. The inlet and outlet chambers were sized to be twice as long in the flow direction as wide (in an axisymmetric model), as can be seen in Figure 1. To set up the models, the inlet diameter was determined from a given porosity based on the hole inlet size, r_1; the actual volumetric porosity was calculated later.

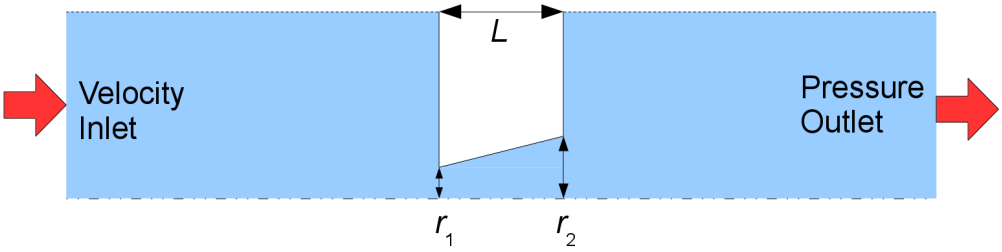

FIG. 1. (Color online) Sketch of the CFD geometry. The axis for this axisymmetric geometry is at the bottom of the sketch, and the upper boundaries are slip-surfaces (symmetry).

The inlet is on the left, where a velocity is specified, and an ambient pressure outlet is on the right. Note that the center-line of the axisymmetric model is at the bottom of the sketch, and the boundaries at the top are non-penetrating, slip surfaces. No slip conditions were imposed on the solid surfaces comprising the hole and the surrounding panel surfaces.

B. CFD Parameters

The CFD calculations were performed using a commercial CFD package based on the finite element method. Since all model dimensions were very small compared to a wavelength at all frequencies of interest, the flow was assumed to be essentially incompressible and isothermal. Twenty computational cells were placed in the radial direction of the hole, with the cell along the axis being four times the size of the cell closest to the wall. Similar cell gradations were used along other edges, to increase the mesh density near the hole. An example section of a typical mesh, near the hole, can be seen in Fig. 2.

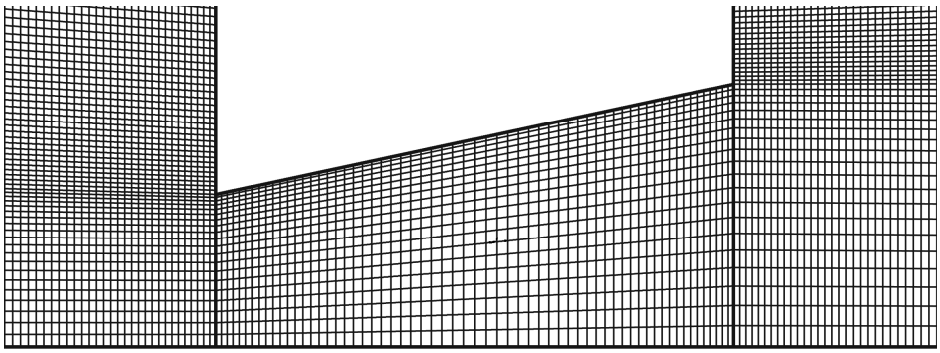

FIG. 2. Typical computational mesh in the region of the perforation.

The inlet velocity was chosen to be a Hann windowed, 5 kHz half-sine having a maximum amplitude, V_0, of 1 mm/s: i.e.,

$$V = V_0 \cdot \frac{1-\cos(4\pi f t)}{2} \cdot \sin(2\pi f t) \quad \text{for} \quad t < \frac{1}{2f} \tag{10}$$

where f was set equal to 5 kHz for all runs. Thus, the inlet velocity was non-zero for the first 100 μs, and equal to zero thereafter.

The inlet velocity profile, as well as its Fourier spectrum, is shown in Fig. 3. There is a node at 20 kHz, but that is outside the frequency range of interest.

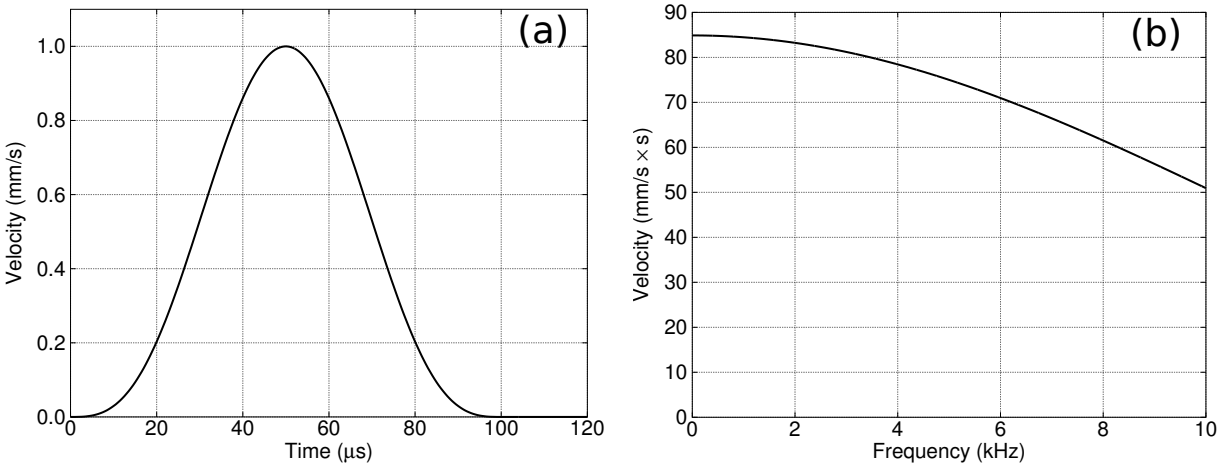

FIG. 3. Inlet velocity as a function of time (a) and the corresponding Fourier spectrum as a function of frequency (b).

In addition to the standard post-processing of CFD results that allows the visualization of the pressure field, the velocity magnitude, and the local shear rate, a local energy loss rate per unit volume can be defined as the product of shear rate, γ, squared and viscosity, η. If integrated over the whole volume, a total energy loss rate, *dE/dt*, is obtained, which is also equal to the overall pressure drop, ΔP, multiplied by the volumetric flux, Q: i.e.,

$$\frac{dE}{dt} = \Delta P \cdot Q = \int_V \eta \cdot \gamma^2 \cdot dV \tag{11}$$

The local energy loss rate, or simply the shear rate, is useful for locating regions of significant energy dissipation.

A fully-coupled solution was obtained with automatic time-stepping which had a maximum time step of 0.5 μs (which was also the data output frequency). In order to obtain accurate low-frequency results that matched steady-state results with less than 2% error, it was necessary to run the model for at least 0.5 ms. Plots of the velocity and pressure versus time or frequency were identical to those shown in Bolton and Kim[35].

Essentially identical results were obtained for a few test cases using another commercial CFD software package based on the finite volume method, as well as a third which solves the linearized acoustic equations in frequency space. Also, it was verified that the direction of flow through a tapered hole made no difference to the results; this was expected since the velocity is low enough to avoid non-linear effects.

IV. END CORRECTIONS FOR STATIC FLOW RESISTANCE

Several series of cases, as specified in Table 1, were run in steady-state to determine the static flow resistances since these runs are more accurate and much faster than those obtained from the low frequency limit of time-dependent runs. The porosity shown is based on the inlet diameter, but the volumetric porosity is greater for conical holes and varied from 1% to over 10%.

Table 1. Parameters defining the steady-state cases.

Series	Thickness mm	Inlet Diameter mm	Angle deg.	Porosity based on Inlet	Number of Cases
Thickness-00-4	0.1 – 2.0	0.4	0	1%	20
Diameter-00-4	0.4	0.05 – 0.60	0	1%	12
Thickness-06-2	0.05 – 1.0	0.2	6	1%	20
Thickness-12-1	0.05 – 1.0	0.1	12	1%	20
Thickness-12-2	0.05 – 1.0	0.2	12	1%	20
Thickness-12-4	0.05 – 1.0	0.4	12	1%	20
Thickness-18-2	0.05 – 1.0	0.2	18	1%	20
Diameter-12-2	0.2	0.05 – 0.40	12	1%	8

A. Straight Holes

The static flow resistance, Z_0, is the limit of the acoustic impedance as the frequency goes to zero. As Maa[1] mentions, the low frequency limit of Eq. 1 is simply the

result obtained from standard Poiseuille flow, without any end effects. So the first step in the present procedure was to determine the end effects for such straight perforations. Whereas Bolton and Kim[35] used an end correction that was appended as an additional term to Maa's equation, it was more convenient here to separate all the factors from the thickness, *L*, and add an end effect to the tube length. Therefore, the losses due to the end effects are equated to an additional hole length, and the end effects do not themselves depend on the film thickness. The relationship was found to be

$$Z_0 = \frac{\Delta P}{V} = \frac{8\,A\,\eta}{\pi\,r^4}(L + 2\beta r) = \frac{8\,\eta}{\sigma\,r^2}(L + 2\beta r) \qquad (12)$$

since the porosity is simply the hole area divided by the periodic (or inlet) area, A: i.e.,

$$\sigma = \pi\,r^2/A \ . \qquad (13)$$

The straight cases were initially used to determine the best fit for the parameter, β. By using the thirty-two straight cases and a least-squares approach to minimize the percent errors, the value for β was found to be 0.616. These end effects are thus simply inversely proportional to the radius cubed. The deviations of the calculated resistances compared to the CFD results were generally less than 1% for these cases.

An example result for a straight hole is shown in Fig. 4, where the flow is from bottom to top. The dominant pressure gradient is constant through the hole, with some fringing at the ends of the hole. The velocity has a uniform parabolic profile within the hole, and is spreading out at both ends. The areas of high shear rate are concentrated along the walls of the hole, but also include a "cap" at each end of the hole where additional losses occur, the so-called "end effects." The energy loss distribution corresponds to the shear rate plot, since it is proportional to shear rate squared. Note that there is no evidence in these figures of energy dissipation by shearing on the planar surfaces around the hole:

rather, the dissipation exterior to the hole (which is thus associated with the resistive end correction) results from shearing within the fluid flow immediately outside the hole.

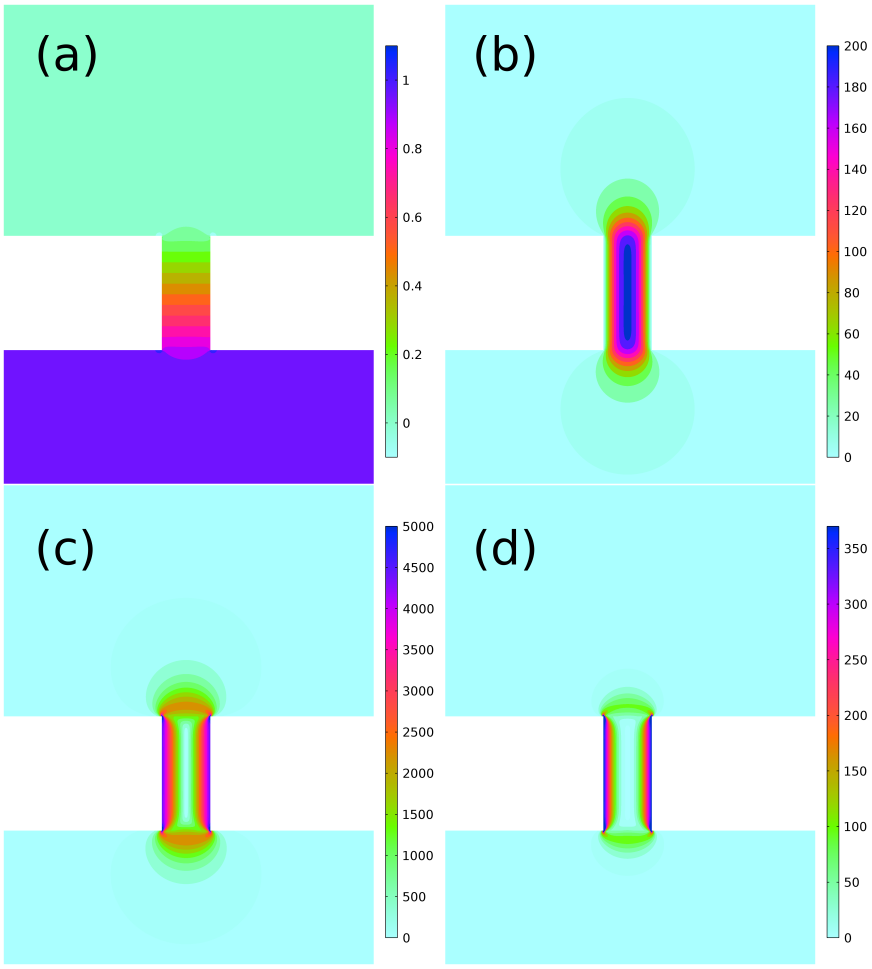

FIG. 4. (Color online) Straight hole steady-state CFD results: (a) pressure field, Pa, (b) velocity magnitude, mm/s, (c) shear rate, 1/s, and (d) energy loss rate, W/m^3. In these images, the flow is from the bottom to the top.

B. Tapered Holes

In the case of slightly tapered holes, for example with angles on one side less than about 20°, an estimate of the pressure drop can be obtained by using Poiseuille flow for a differential length, integrating through the hole, and adding on end effects. Since the end effects were just determined to be inversely proportional to the radius cubed, each of the

two ends of the tapered tube, with radii r_1 and r_2, will now have a different contribution. The resulting resistance can thus be written as follows:

$$Z_0 = \frac{\Delta P}{V} = \frac{8\,A\,\eta}{\pi\, r_1^3\, r_2^3}\left[\frac{L}{3}(r_1^2 + r_1 \cdot r_2 + r_2^2) + \beta(r_1^3 + r_2^3)\right] . \qquad (14)$$

However, it was observed that a small deviation still remained, up to 7% for some of the 18° cases. These deviations are approximately proportional to the taper angle, θ, defined by

$$\tan(\theta) = (r_2 - r_1)/L \ . \qquad (15)$$

They can be corrected by using a simple modification of the previous formula: i.e.,

$$Z_0 = \frac{\Delta P}{V} = \frac{8\,A\,\eta}{\pi\, r_1^3\, r_2^3}\left[\frac{L}{3}(r_1^2 + r_1 \cdot r_2 + r_2^2) + \beta\left(\frac{\pi - 2\theta}{\pi} r_1^3 + \frac{\pi + 2\theta}{\pi} r_2^3\right)\right] . \qquad (16)$$

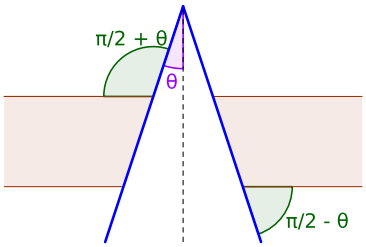

FIG. 5. (Color online) Sketch of relevant geometry for understanding the taper angle terms in Eq. 16. The ratio of the entrance (and exit) angle to 90º (i.e. π/2) enters into the equation.

This formulation increases the end effect for the smaller end of the perforation. Conceptually, see Fig. 5, one can think that flow exiting (or entering) a straight hole needs to turn up to 90° as it spreads out. For a tapered hole, the flow would need to turn additionally up to the taper angle for the small end, and that much less for the large end. By using all one hundred and forty cases and a least-squares approach to minimize the percent errors, an empirical value for β was found to be:

$$\beta = 0.613 \ . \tag{17}$$

Figure 6 shows the CFD results for a tapered hole. The pressure gradient as well as the velocity is greatest near the small end of the taper. Correspondingly, the shear rates and energy losses are also greatest in the same region. In particular, if the hole is long enough, only the end effect at the small end is relevant for the static flow resistance.

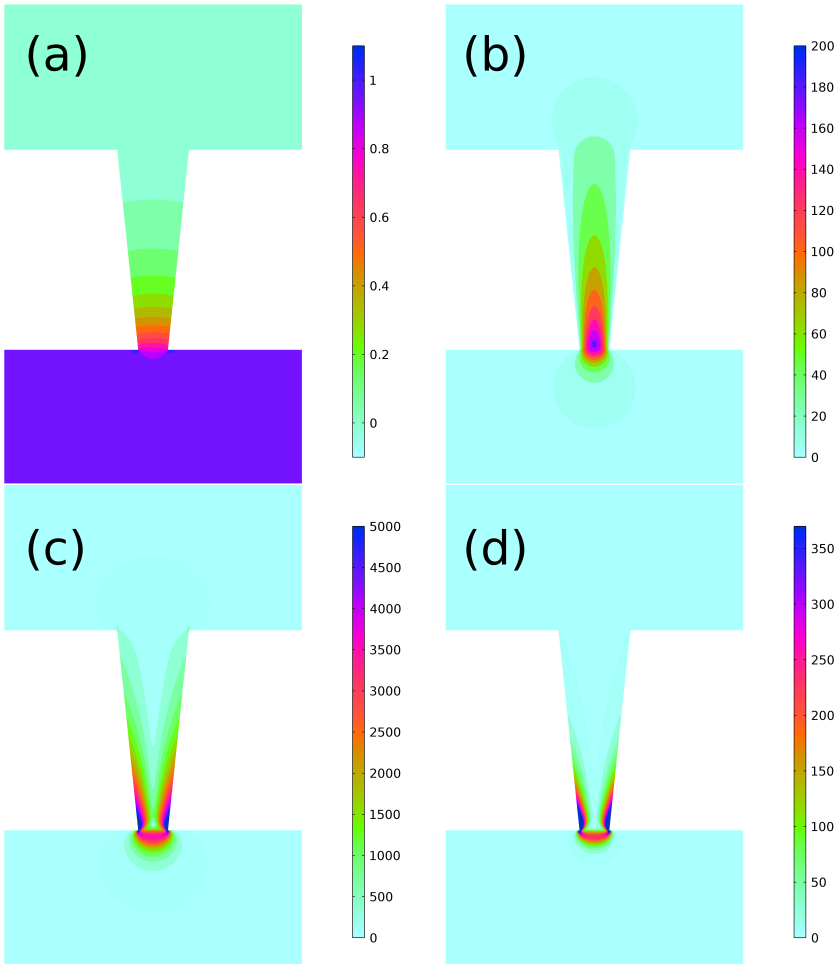

FIG. 6. (Color online) Tapered hole steady-state CFD results: (a) pressure field, Pa, (b) velocity magnitude, mm/s, (c) shear rate, 1/s, and (d) energy loss rate, W/m^3. In these images, the flow is from the bottom to the top.

When comparing the results from Eq. 16 to the CFD results, the resistance generally matches to within 1%. One can eliminate the periodic area, A, by using the porosity as was

done previously. Since the porosity is the volume fraction of the panel which the holes occupy, one has

$$\sigma = \frac{V_{hole}}{A \cdot L} = \frac{\pi}{3A}(r_1^2 + r_1 \cdot r_2 + r_2^2) \ . \tag{18}$$

This relation can be used to eliminate the area in Eq. 16, if desired.

In Figure 7, the pressure drops of the one hundred and forty cases obtained using CFD are compared with the various formulae. The results show that the Poiseuille flow estimate, for tapered holes but without end effects, is not sufficient (Eq. 14 with β=0, circles). Since Maa's and Guo's formulae have a static flow resistance matching that for Poiseuille flow, their values of dynamic flow resistance are also too small at low frequencies. When the present empirical end corrections for straight holes are included, the CFD results are almost matched (Eq. 14 with β=0.613, squares). Finally, after modifying the end corrections for the taper angle, the concluding expression (Eq. 16 with β=0.613, diamonds) can be seen to fall directly on the diagonal (line), as desired.

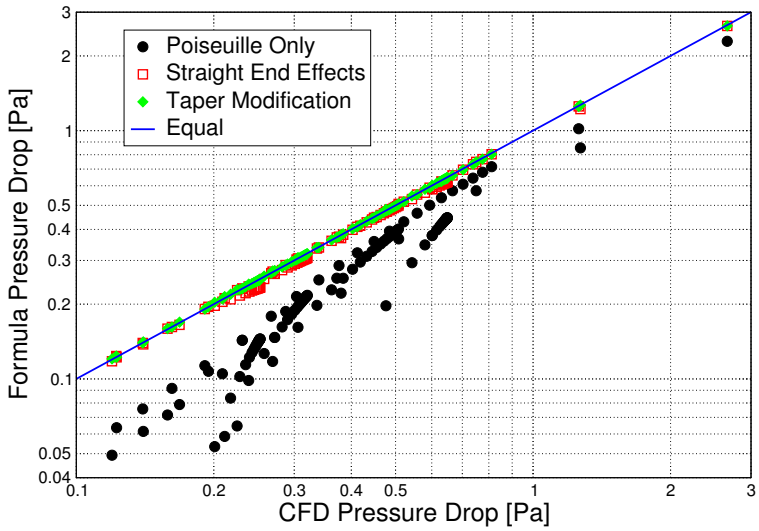

FIG. 7. (Color online) Comparison of one hundred and forty steady-state CFD pressure drop results with the three formulae discussed in the text.

C. Equal Cases

By using this new empirical formula, Eq. 16, eight cases were created (see Table 2), all with an expected static pressure drop of 1 Pa for a face velocity of 1 mm/s, and therefore with an expected static flow resistance of 1000 kg/m^{2}s, commonly referred to as MKS Rayls.

Table 2. Parameters defining eight cases expected to have equal static flow resistance.

Case #	Thickness mm	Inlet Diameter mm	Angle deg.	Porosity based on Inlet	Volumetric Porosity
1	0.7	0.21852	0	1.0%	1.00%
2	0.4	0.16991	0	1.0%	1.00%
3	0.1	0.09524	0	1.0%	1.00%
4	0.7	0.15061	0	2.0%	2.00%
5	0.7	0.10422	6	1.0%	3.08%
6	0.2	0.08678	6	1.0%	1.56%
7	0.7	0.12799	12	0.5%	2.56%
8	0.2	0.11796	12	0.5%	0.95%

The pressure drops calculated using CFD for all eight cases were in the range 0.9965-1.0083 Pa, showing the accuracy of the formula. It can be seen that the same static flow resistance can be achieved by either straight or tapered holes. As thickness is reduced in straight holes, the hole diameter must be reduced as well. However, for tapered holes, this reduction is very minor, because most of the losses occur at the small end of the hole and the pressure drop is not very sensitive to the details at the large end.

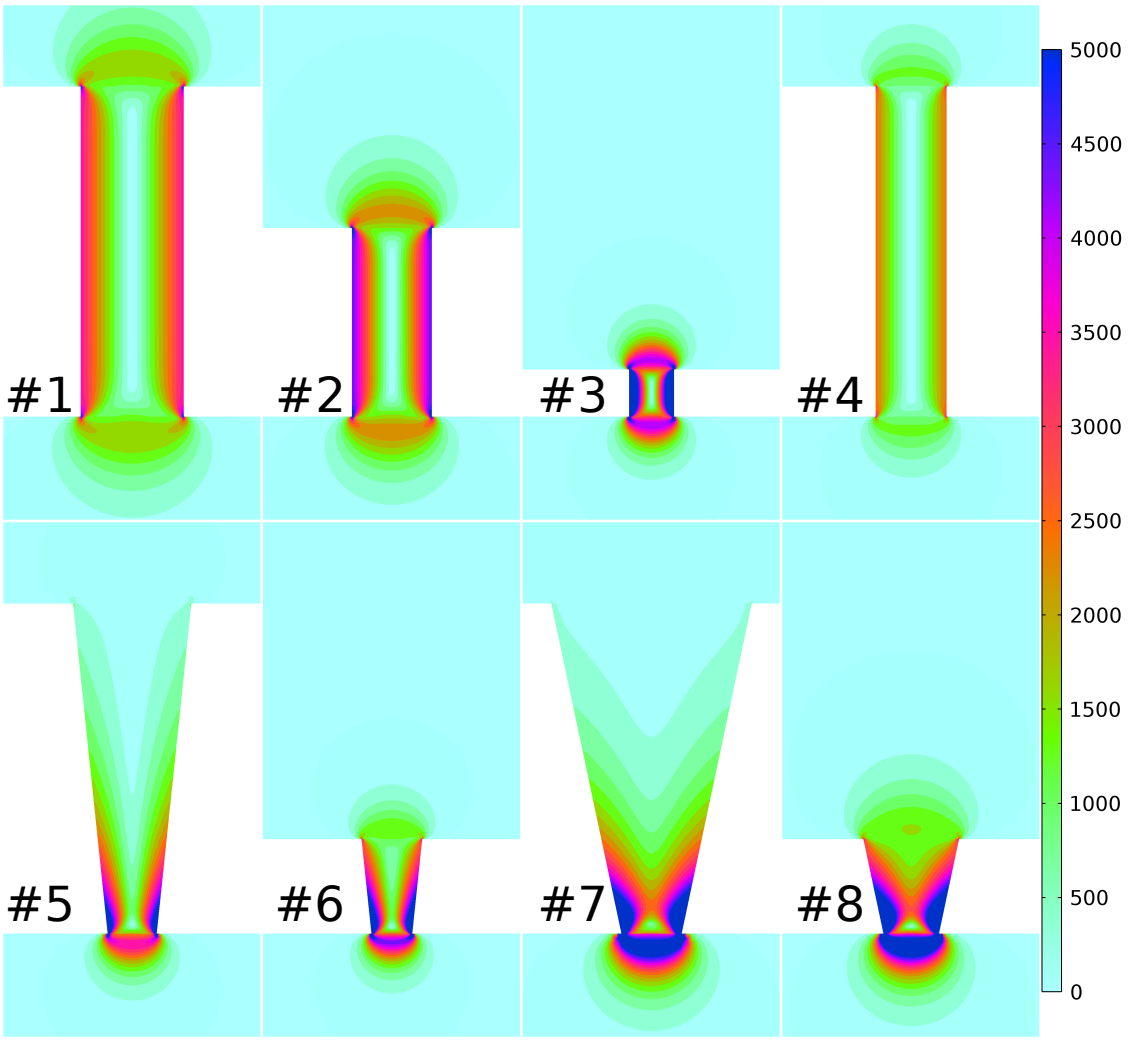

FIG. 8. (Color online) This series of images shows the shear rate (1/s) for the eight cases listed in Table 2.

Figure 8 shows the shear rate for all eight cases from Table 2. The energy losses, which are proportional to the shear rate squared, are clearly lower for case 4, which has twice the porosity, and higher for the last two cases which have half the porosity and need more loss per hole. The tapered cases clearly show how most of the losses are concentrated at the small end, thus making the total length relatively unimportant.

V. DYNAMIC FLOW RESISTANCE

The acoustic transfer impedance of the panel was calculated as

$$Z_{CFD} = (P_{in} - P_{out}) \,/\, V_{in} \tag{19}$$

where P_{in} is the inlet pressure, P_{out} is the outlet pressure (ambient), and V_{in} is the inlet velocity (see Fig. 3); all of these quantities were first Fourier transformed in order to obtain the impedance in the frequency domain. The real part of the impedance is referred to here as the dynamic flow resistance, and the imaginary part as the reactance.

For these time-dependent studies, several series of cases were run, as specified in Table 3, including both straight and tapered holes. The porosity shown is based on the inlet diameter, but the volumetric porosity is greater for conical holes and varied from 0.5% to 7%.

Table 3. Parameters defining the time-dependent cases.

Series	Thickness mm	Inlet Diameter mm	Angle deg.	Porosity based on Inlet	Number of Cases
Thickness-00-4	0.1 – 1.0	0.4	0	1%	5
Diameter-00-2	0.2	0.05 – 0.40	0	1%	5
Diameter-00-7	0.7	0.05 – 0.40	0	1%	5
Diameter-06-2	0.2	0.05 – 0.40	6	1%	5
Diameter-06-7	0.7	0.05 – 0.40	6	1%	5
Diameter-12-2	0.2	0.05 – 0.40	12	1%	5
Diameter-12-7	0.7	0.10 – 0.40	12	1%	4
Porosity	0.2	0.2	0 – 12	0.5 – 2.0%	6
Equal		*From Table* 2			8

The pressure time history for two example cases can be seen in Fig. 9. Note that for the tapered case the results are essentially independent of flow direction. It should also be noted that the pressure remains below zero for a substantial time after the inlet flow has already stopped (at 100 μs).

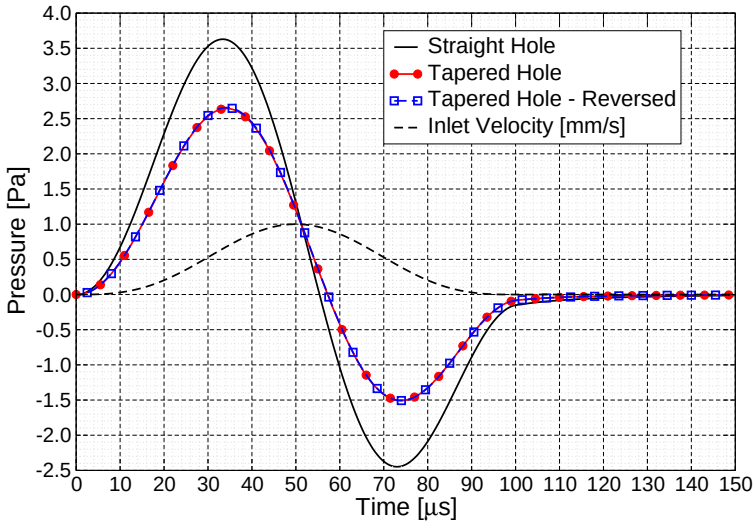

FIG. 9. (Color online) Inlet pressure from the CFD calculations for cases 2 ("Straight") and 5 ("Tapered") of Table 2. The tapered hole was run with flow in both directions, and it can be seen that the two curves are practically on top of each other. The velocity is shown simply for timing reference.

A. Tapered Holes without End Corrections

For the dynamic resistance, the same formulation as for the static flow resistance can be used by considering a differential form of Maa's expression (Eq. 1) for a thin slice of the hole, and integrating this through the thickness of the film, i.e.,

$$Z_{Taper} = j\rho\omega \int_0^L \frac{1}{\sigma_x}\left[1 - \frac{2}{k_x\sqrt{-j}}\frac{J_1\left(k_x\sqrt{-j}\right)}{J_0\left(k_x\sqrt{-j}\right)}\right]^{-1} dx \qquad (20)$$

where now r, k and σ vary with position, x, through the hole: i.e.,

$$\begin{aligned} r_x &= r_1 + (r_2 - r_1)\, x/L \\ k_x &= r_x\sqrt{\omega\rho/\eta} \\ \sigma_x &= \pi\, r_x^2/A \quad . \end{aligned} \qquad (21)$$

The perforation constant varies linearly through the hole, and the varying porosity accounts for the changing mean velocity within the hole resulting from the area change. In practice, this integral can be computed numerically, for each frequency point. For straight holes

Eq. 20 reduces to Eq. 1.

This expression accounts for the losses within a tapered hole, but it does not yet include end corrections. The zero frequency limit of this expression matches Eq. 16 with $\beta = 0$.

B. Straight Hole Dynamic End Corrections

For straight holes, it is possible to modify Eq. 1 to include end effects initially for the static and now for the dynamic flow resistances by dividing by the thickness and multiplying by the thickness plus end effects:

$$Z = \frac{L + \beta d}{L} Z_{Maa} \ . \tag{22}$$

This expression is more accurate for low frequencies than previous studies (e.g., Eq. 1, Eq. 6, or even Eq. 9). For some cases, this expression almost exactly matches the CFD results, whereas for other cases it may deviate as much as 10% at 10 kHz. Further research may be needed to determine a satisfactory expression for a small additional dynamic end correction for straight holes. Nonetheless, the current modification, Eq. 22, is an improvement to the accuracy when predicting the performance of straight holes and can be used as a design tool for such cases (see Figure 10a). It should be noted that this modification is applied to the complex impedance and thereby changes both the resistance and the reactance.

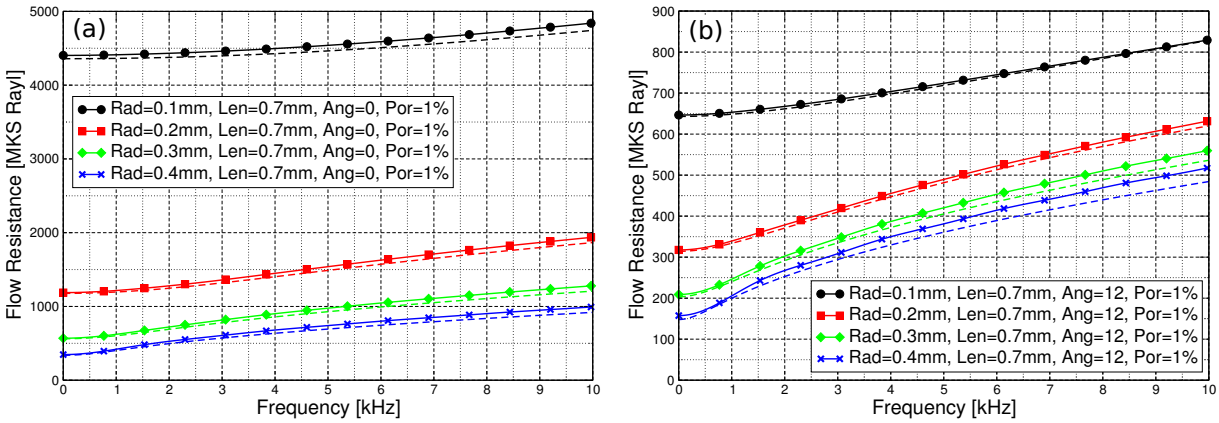

FIG. 10. (Color online) Dynamic flow resistances for 4 cases with straight holes (a) and 4 cases with tapered holes (b). CFD results (solid) are compared with results from Eq. 23 (dashed).

The time evolution of velocity and shear rate can be seen in Fig. 11. The velocity increases uniformly to its peak value while the high shear remains near the wall. However, as the flow slows down, the central flow is faster than it would be for an equivalent steady flow, and the region near the walls slows down to a greater extent. Even when the mean flow is 0 (after 100 μs), there is a reverse flow near the wall with a forward flow in the middle of the channel. The region of highest shear rate also migrates from the wall toward the middle of the channel as the flow decelerates.

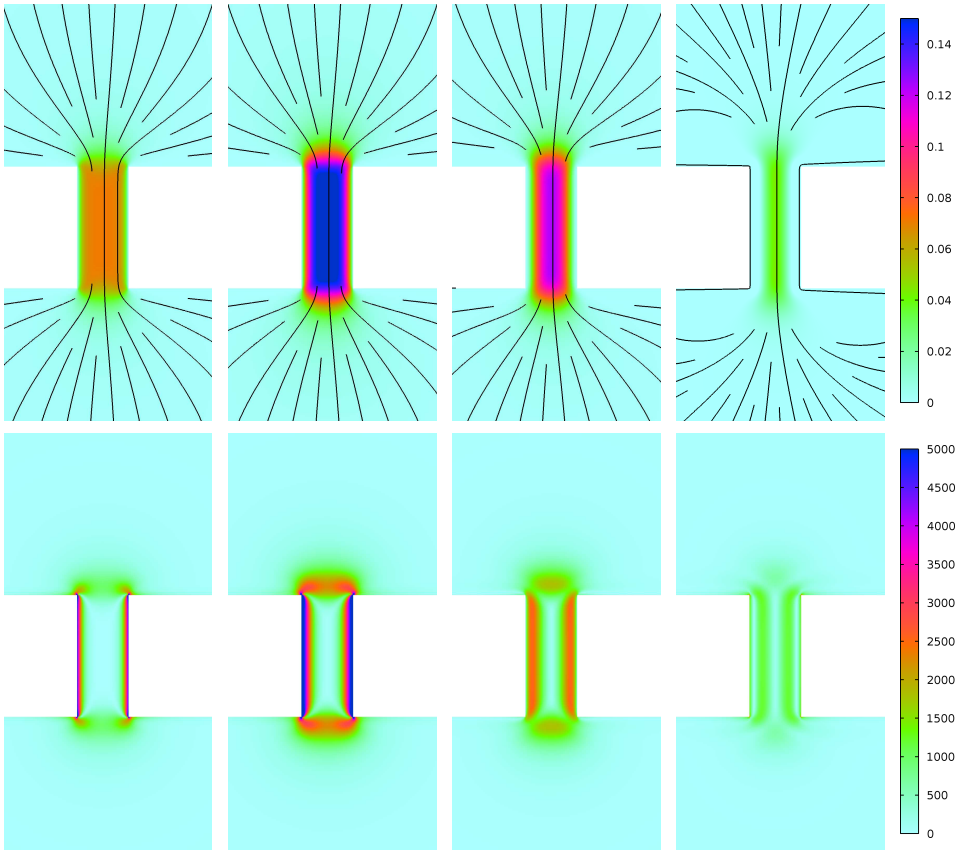

FIG. 11. (Color online) For a straight case (#2 in Table 2) the velocity magnitude (m/s) is shown in the upper row and the corresponding shear rate (1/s) is shown in the lower row. The times from left to right are at 30, 50, 70, and 90 μs.

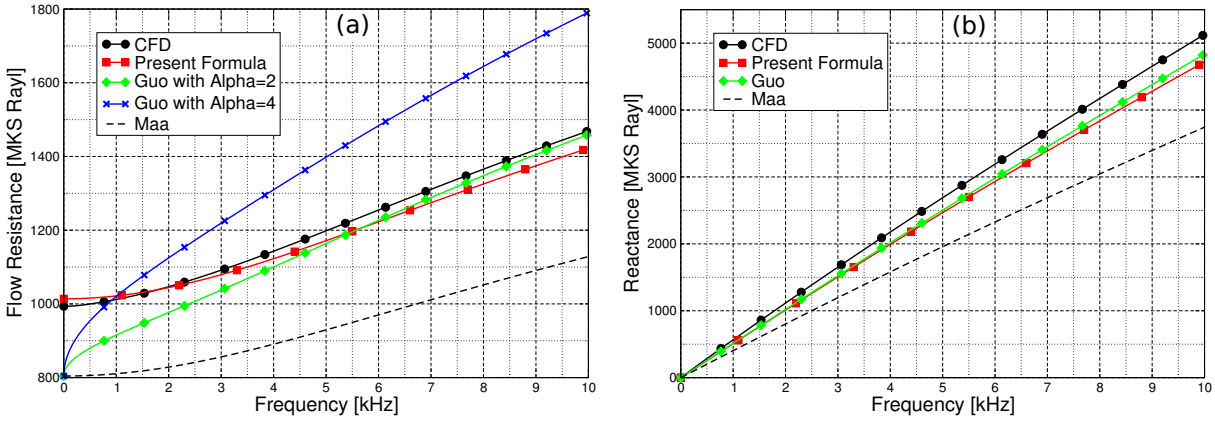

FIG. 12. (Color online) Resistance (a) and reactance (b) plots for a straight case (#2 from Table 2). Corresponding formula results using Eq. 22, Eq. 1 (Maa) and Eq. 6 (Guo) with α=2 and α=4 are shown as well.

A comparison of the present formula (Eq. 22) and those of Maa and Guo (Eqs. 1 and 6 in the present article respectively), with $\alpha = 2$ and $\alpha = 4$, can be seen in Fig. 12. For resistance, Guo's formula, with α=2 not 4, works well above 5 kHz, but deviates significantly from the CFD results at lower frequencies. Both the present formula as well as Guo's formula work well for estimating the reactance.

C. Tapered Hole Dynamic End Corrections

For tapered holes, the expression becomes more complicated, but the concept is the same as for the straight holes: i.e., divide by the thickness term and multiply by the thickness with the static flow resistance end effects, Eq. 16, included to give:

$$Z_* = \frac{\frac{L}{3}(r_1^2 + r_1 \cdot r_2 + r_2^2) + \beta \cdot \left(\frac{\pi - 2\theta}{\pi} r_1^3 + \frac{\pi + 2\theta}{\pi} r_2^3\right)}{\frac{L}{3}(r_1^2 + r_1 \cdot r_2 + r_2^2)} \cdot Z_{Taper} \qquad (23)$$

where Z_{Taper} is given by the integrated Maa expression, Eq. 20. For straight holes, Eq. 23 reduces to Eq. 22. This new expression is accurate for low frequencies (starting at the static flow resistance) and is reasonable for other frequencies of interest, giving designers predictive capabilities for tapered holes. See Figure 10b for a comparison of CFD results with those of Eq. 23.

The velocity magnitude and shear rate through tapered holes can be seen in Fig. 13. Many of the trends mentioned for straight holes apply here as well, but are now concentrated at the narrow end of the taper.

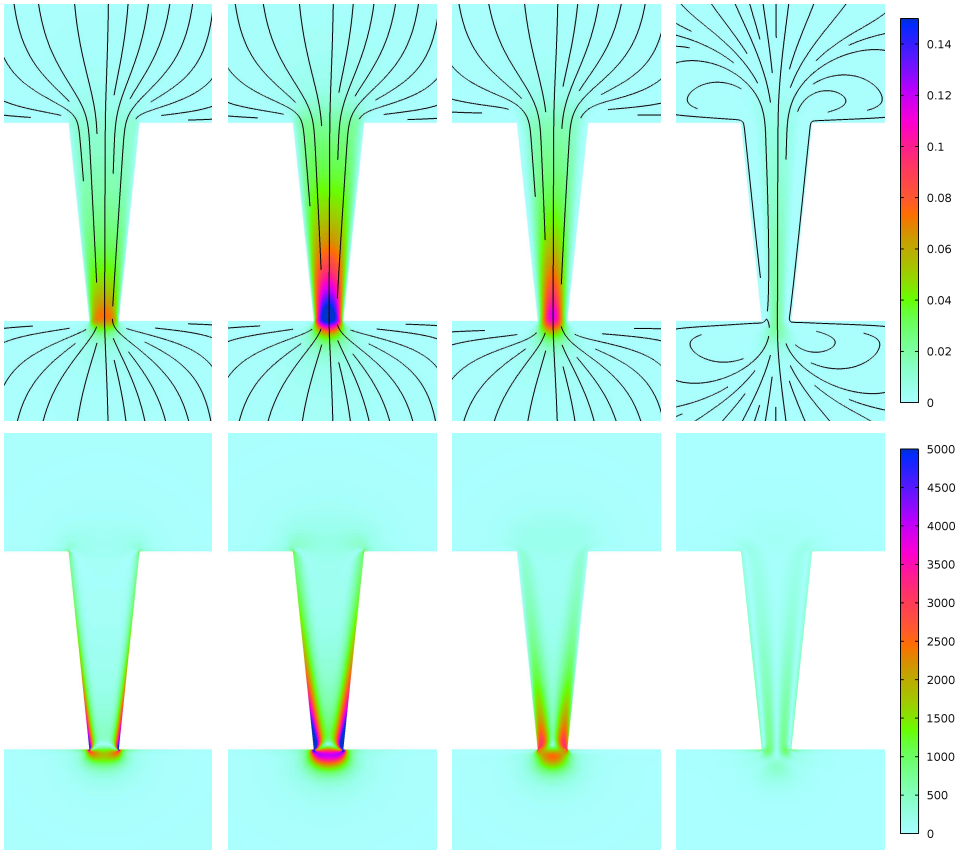

FIG. 13. (Color online) For the tapered case (#5 in Table 2) the velocity magnitude (m/s) is shown in the upper row and the corresponding shear rate (1/s) is shown in the lower row. The times from left to right are at 30, 50, 70, and 90 μs.

The impedance from the CFD calculations for the tapered and straight holes is compared to the present formula in Fig. 14. It is also possible to see a minor difference between the forward and reverse flow for the tapered geometry due to very small non-linear effects captured by the CFD computation.

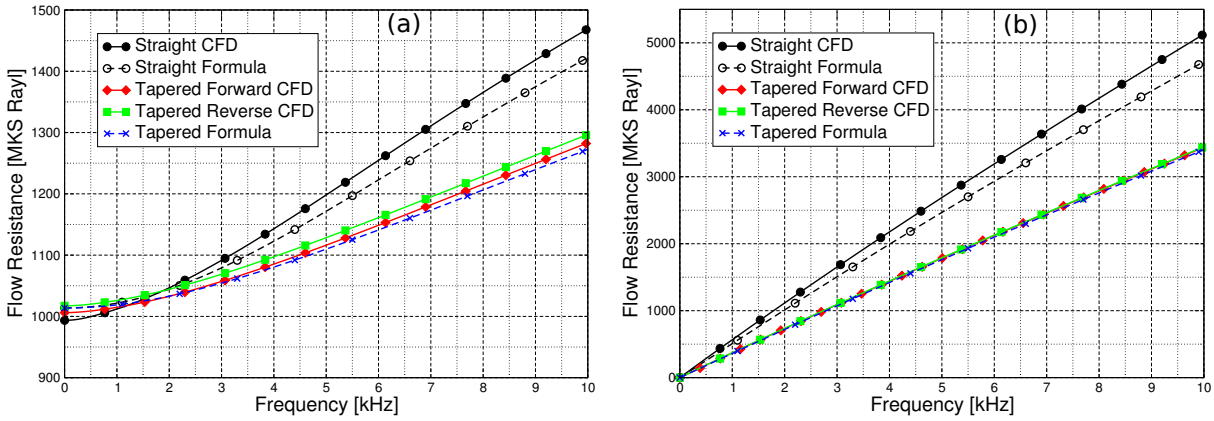

FIG. 14. (Color online) Resistance (a) and reactance (b) plots for straight and tapered cases (#2 and #5 from Table). Corresponding formula results using Eq. 23 are shown as well. Only a slight difference between forward and reverse flow can be seen in the resistance plot.

VI. CASES HAVING EQUIVALENT STATIC FLOW RESISTANCE

A. Dynamic Flow Resistance

It is instructive to look at the eight cases with equal static flow resistance, from Table 2, in more detail. Even though the static flow resistances are equal, the dynamic flow resistances are not: see, for example Fig. 15. Nonetheless, several pairs of cases have essentially equal responses, showing that different geometries can have the same dynamic response (e.g., pairs 3 and 6, 2 and 7, and 4 and 8), but that this can't be predicted from the static flow resistance alone. Chevillotte[18] has previously noted that the sound absorption offered by a microperforated panel varies when the hole diameter and porosity are changed while keeping the static flow resistance equal to the characteristic impedance of air. Here we show similar behavior, seen in the resistance and absorption plots, for both straight and tapered holes.

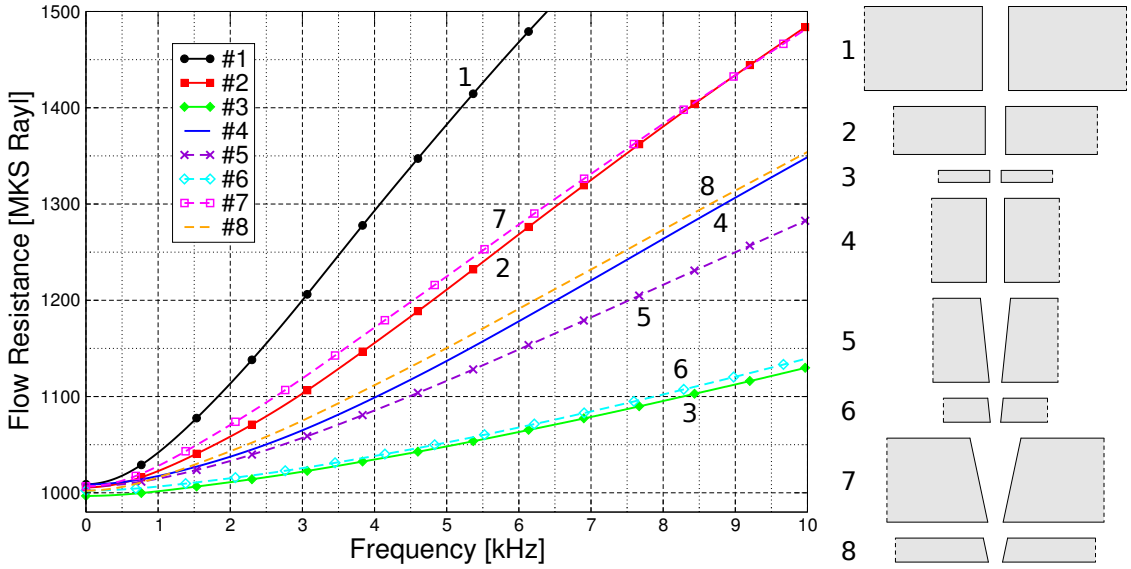

FIG. 15. (Color online) Dynamic flow resistances for cases with equal static flow resistance, from Table 2. Sketches of the eight hole designs, all on equal scales, are shown so the length and diameter of the holes can better be compared; additionally, the horizontal extent of the film (shown shaded) gives an indication of the hole density.

B. Absorption Coefficient

If a backing depth, D, behind the perforated film, is considered, the surface normal impedance of the film and a rigidly terminated air space can be computed as

$$Z_p = Z - j\rho c \cdot \cot(\omega D/c) \tag{24}$$

where c is the speed of sound, and Z is the transfer impedance of the microperforated sheet. The normal incidence plane wave reflection coefficient is then

$$R = \left(Z_p - \rho c\right)/\left(Z_p + \rho c\right) \tag{25}$$

and the normal incidence absorption coefficient can be defined as:

$$\alpha = 1 - |R|^2 \ . \tag{26}$$

Figure 16a shows these absorption coefficients calculated from the CFD results for the cases from Table 2. The peak absorption and node locations remain roughly constant

for the eight cases. However, there is a wide range of absorption characteristics; for example at a frequency of 2.0 kHz, the absorption varies from 32% to 74% among the cases.

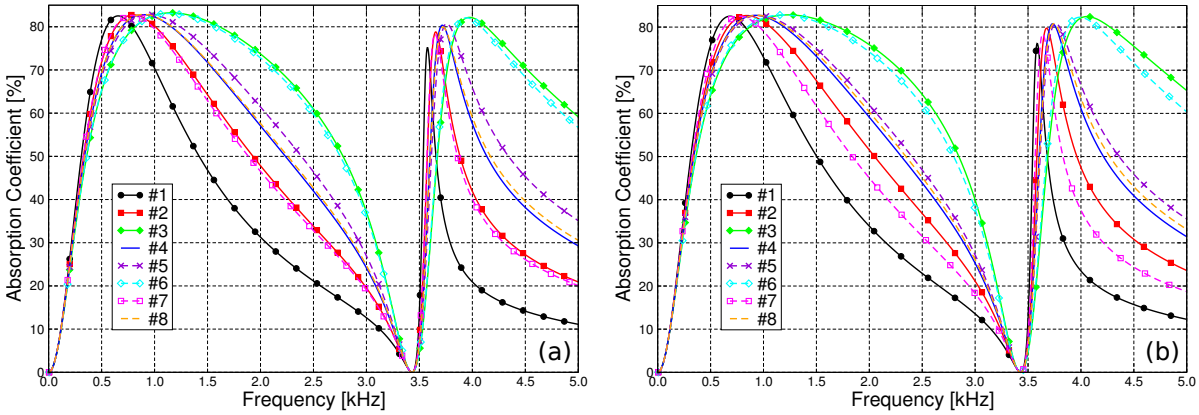

FIG. 16. (Color online) Absorption coefficients for cases with equal static flow resistance, from Table 2, and a rigidly terminated air space of 25 mm. Graph (a) shows results using the impedance from the CFD calculations, and graph (b) shows the results using the impedance from Eq. 23.

The formula results, plotted in Figure 16b, are a very close match to the CFD results seen in Fig. 16a, and show all the major trends. Further research will be needed to determine taper hole design geometries of perforated films to meet acoustical and manufacturing requirements and constraints for specific applications.

VII. CONCLUSIONS

In this paper, CFD models of microperforated materials with straight and tapered holes have been considered. These models produce results that generally conform to well-established theoretical models. However, the CFD models have been used to generate an expression (Eq. 23) that more accurately captures the dynamic flow resistance at low frequencies for straight holes and for tapered hole geometries. For this study only sharp-

edged holes with taper angles from 0° to 20° were considered. The simple linear dependence on angle introduced here may be more complex for larger angles, and the assumption of one-dimensional flow through the hole, allowing the integration of Maa's formula, would also break down. It was found that the added terms accounting for the end effects of both straight and tapered holes don't depend on film thickness, only on the two diameters at the ends of the holes. It was also shown that straight and tapered hole geometries can have equal static flow resistances, and that even though it is possible for such geometries to have essentially equal dynamic flow resistances, this is not always the case. In other words, it's possible for straight and tapered hole geometries with equal static flow resistance to have different dynamic flow resistances and different absorption coefficients.

In future work it would be useful to confirm the assumption that the compressibility of the fluid (and hence, heat transfer to the solid phase) does not need to be accounted for in the CFD calculations. In addition, the effect of panel mass and flexibility on the flow profiles within the holes should be examined since panel motion may be significant when the microperforated panel mass per unit area is very small, as can be the case for polymeric microperforated films.

REFERENCES

[1]D.Y. Maa, “Theory and design of microperforated panel sound-absorbing constructions,” Scientia Sinica, **18**(1), 55-71 (1975).

[2]D.Y. Maa, “Microperforated-panel wideband absorbers,” Noise Control Engineering Journal **29**(3), 77-84 (1987).

[3]D.Y. Maa, “Potential of microperforated panel absorber,” Journal of the Acoustical Society of America, **104**(5), 2861-2866 (1998).

[4]T. Yoo, J.S. Bolton, J.H. Alexander and D.F. Slama, “An improved model for micro-perforated absorbers,” Proceedings of NOISE-CON 2007, 1654-1661 (2007).

[5]I. B. Crandall, Theory of Vibrating Systems and Sound (Van Nostrand, New York) pp. 229 (1926).

[6]U. Ingard, “On the theory and design of acoustic resonators,” Journal of the Acoustical Society of America, **25**(6), 1037-1061 (1953).

[7]H.V. Fuchs and X.Q. Zha, “Microperforated structures as sound absorbers - A review and outlook,” Acta Acustica united with Acustica **92**(1), 139-146 (2006).

[8]S. Allam, Y. Guo, and M. Åbom, “Acoustical study of micro-perforated plates for vehicle applications,” SAE Technical Paper 2009-01-2037 (2009).

[9]K. Sakagami, M. Yairi and M. Morimoto, “Multiple leaf sound absorbers with microperforated panels: An overview,” Acoustics Australia **38**(2), 76 -81 (2010).

[10]M.Q. Wu. “Micro-perforated panels for duct silencing,” Noise Control Engineering Journal, **45**(2), 69-77 (1997).

[11]J. Liu, D.W. Herrin, and A.F. Seybert, “Application of micro-perforated panels to attenuate noise in a duct,” SAE Technical Paper 2007-01-2196 (2007).

[12]J. Liu and D.W. Herrin, “Enhancing micro-perforated panel attenuation by partitioning the adjoining cavity,” Applied Acoustics, **71**(2), 120-127 (2010).

[13]S. Allam and M. Åbom, “A new type of muffler based on microperforated tubes,” Journal of Vibration and Acoustics – Transactions of the ASME **133**(3) Article Number: **031005** (2011).

[14]H.J. Shin and J.S. Bolton, “Microperforated materials as duct liners: local reaction *versus* extended reaction backings,” Proceedings of NOISE-CON 2011, 748-760 (2011).

[15]S. Allam and M. Abom, “Noise control for cooling fans on heavy vehicles,” Noise Control Engineering Journal **60**(6), 707-715 (2012).

[16]A. Viswanathan and J.S. Bolton, “Study of the effect of grazing flow on the performance of microperforated and perforated panels,” Proceedings of NOISE-CON 2013 (2013).

[17]A. Parrett, C. Wang, X. Zeng, D. Nielubowicz, M. Snowden, J.H. Alexander, R.W. Gerdes, B. Leeder and C. Zupan, "Application of micro-perforated composite acoustic material to a vehicle dash mat," SAE Technical Paper 2011-01-1623 (2011).

[18]F. Chevillotte, “Controlling sound absorption by an upstream resistive layer,” Applied Acoustics, **73**(1), 56-60 (2012).

[19]D. Takahashi, K. Sakagami and M. Morimoto, “Acoustic properties of permeable membranes,” Journal of the Acoustical Society of America **99**(5), 3003-3009 (1996).

[20]K. Sakagami, M. Kiyama, M. Morimoto and D. Takahashi, “Detailed analysis of the acoustic properties of a permeable membrane,” Applied Acoustics **54**(2), 93-111 (1998).

[21]K. Sakagami, M. Morimoto and M. Yairi, “A note on the effect of vibration of microperforated panel on its sound absorption characteristics,” Acoustical Science and Technology, **26**(2), 204-207 (2005).

[22]J. Song and J.S Bolton, “Acoustical modeling of tensioned, permeable membranes,” Proceedings of NOISE-CON 2003, 965-970 (2003).

[23]J. Song and J.S. Bolton, “Sound absorption characteristics of membrane-based sound absorbers,” Proceedings of INTER-NOISE 2003, 3881-3888 (2003).

[24]T. Yoo, J.S. Bolton, J.H. Alexander and D.F. Slama, “Absorption from finite-size microperforated panels at arbitrary incidence angles,” Proceedings of the 15th International Congress on Sound and Vibration, Daejeon, Korea (2008).

[25]M. Toyoda, R.L. Mu and D. Takahashi, “Relationship between Helmholtz-resonance absorption and panel-type absorption in finite flexible microperforated-panel absorbers,” Applied Acoustics **71**(4), 315-320 (2010).

[26]T. Yoo, J.S. Bolton, J.H. Alexander and D.F. Slama, “Absorption of finite-sized micro-perforated panels with finite flexural stiffness at normal incidence,” Proceedings of NOISE-CON 2008, 1102-1113 (2008).

[27]T. Bravo, C. Maury and C. Pinhede, “Sound absorption and transmission through flexible micro-perforated panels backed by an air layer and a thin plate,” Journal of the Acoustical Society of America,” **131**(5), 3853-3863 (2012).

[28]T. Bravo, C. Maury and C. Pinhede, “Vibroacoustic properties of thin micro-perforated panel absorbers,” Journal of the Acoustical Society of America, **132**(2), 789-798 (2012).

[29]Y. Guo, S. Allam, and M. Åbom, “Micro-perforated plates for vehicle applications,” Proceedings of INTER-NOISE 2008, 1918-1936 (2008).

[30]R.T. Randeberg, “Perforated panel absorbers with viscous energy dissipation enhanced by orifice design,” Ph.D. Thesis, Department of Telecommunications, Norwegian University of Science and Technology, Trondheim (2000).

[31]K. Sakagami, M. Morimoto, M. Yairi, and A. Minemura, “A pilot study on improving the absorptivity of a thick microperforated panel absorber,” Applied Acoustics, **69**(2), 179-182 (2008).

[32]T.E. Vigran, “Conical apertures in panels; Sound transmission and enhanced absorption in resonator systems,” Acta Acustica united with Acustica, **90**(6), 1170-1177 (2004).

[33]N. Atalla and F. Sgard, “Modeling of perforated plates and screens using rigid frame porous models,” Journal of Sound and Vibration **303**(1-2), 195-208 (2007).

[34]K. Hou and J.S. Bolton, “Finite element models for micro-perforated materials,” Proceedings of INTER-NOISE 2009, 2420-2428 (2009).

[35]J.S. Bolton and N. Kim, “Use of CFD to calculate the dynamic resistive end correction for micro-perforated materials,” Acoustics Australia, **38**, 134-139 (2010).

[36]K. Hou and J.S. Bolton, “Validation of micro-perforated panel models,” Proceedings of INTER-NOISE 2008, 2414-2420 (2008).

Table 1

Table 1. Parameters defining the steady-state cases.

Series	Thickness mm	Inlet Diameter mm	Angle deg.	Porosity based on Inlet	Number of Cases
Thickness-00-4	0.1 – 2.0	0.4	0	1%	20
Diameter-00-4	0.4	0.05 – 0.60	0	1%	12
Thickness-06-2	0.05 – 1.0	0.2	6	1%	20
Thickness-12-1	0.05 – 1.0	0.1	12	1%	20
Thickness-12-2	0.05 – 1.0	0.2	12	1%	20
Thickness-12-4	0.05 – 1.0	0.4	12	1%	20
Thickness-18-2	0.05 – 1.0	0.2	18	1%	20
Diameter-12-2	0.2	0.05 – 0.40	12	1%	8

Table 2

Table 2. Parameters defining eight cases expected to have equal static flow resistance.

Case #	Thickness mm	Inlet Diameter mm	Angle deg.	Porosity based on Inlet	Volumetric Porosity
1	0.7	0.21852	0	1.0%	1.00%
2	0.4	0.16991	0	1.0%	1.00%
3	0.1	0.09524	0	1.0%	1.00%
4	0.7	0.15061	0	2.0%	2.00%
5	0.7	0.10422	6	1.0%	3.08%
6	0.2	0.08678	6	1.0%	1.56%
7	0.7	0.12799	12	0.5%	2.56%
8	0.2	0.11796	12	0.5%	0.95%

Table 3

Table 3. Parameters defining the time-dependent cases.

Series	Thickness mm	Inlet Diameter mm	Angle deg.	Porosity based on Inlet	Number of Cases
Thickness-00-4	0.1 – 1.0	0.4	0	1%	5
Diameter-00-2	0.2	0.05 – 0.40	0	1%	5
Diameter-00-7	0.7	0.05 – 0.40	0	1%	5
Diameter-06-2	0.2	0.05 – 0.40	6	1%	5
Diameter-06-7	0.7	0.05 – 0.40	6	1%	5
Diameter-12-2	0.2	0.05 – 0.40	12	1%	5
Diameter-12-7	0.7	0.10 – 0.40	12	1%	4
Porosity	0.2	0.2	0 – 12	0.5 – 2.0%	6
Equal		*From Table* 2			8

Figure Captions

FIG. 1. (Color online) Sketch of the CFD geometry. The axis for this axisymmetric geometry is at the bottom of the sketch, and the upper boundaries are slip-surfaces (symmetry).

FIG. 2. Typical computational mesh in the region of the perforation.

FIG. 3. Inlet velocity as a function of time (a) and the corresponding Fourier spectrum as a function of frequency (b).

FIG. 4. (Color online) Straight hole steady-state CFD results: (a) pressure field, Pa, (b) velocity magnitude, mm/s, (c) shear rate, 1/s, and (d) energy loss rate, W/m^3. In these images, the flow is from the bottom to the top.

FIG. 5. (Color online) Sketch of relevant geometry for understanding the taper angle terms in Eq. 16. The ratio of the entrance (and exit) angle to 90º (i.e. $\pi/2$) enters into the equation.

FIG. 6. (Color online) Tapered hole steady-state CFD results: (a) pressure field, Pa, (b) velocity magnitude, mm/s, (c) shear rate, 1/s, and (d) energy loss rate, W/m^3. In these images, the flow is from the bottom to the top.

FIG. 7. (Color online) Comparison of one hundred and forty steady-state CFD pressure drop results with the three formulae discussed in the text.

FIG. 8. (Color online) This series of images shows the shear rate (1/s) for the eight cases listed in Table 2.

FIG. 9. (Color online) Inlet pressure from the CFD calculations for cases 2 (“Straight”) and 5 (“Tapered”) of Table 2. The tapered hole was run with flow in both directions, and it can be seen that the two curves are practically on top of each other. The velocity is shown simply for timing reference.

FIG. 10. (Color online) Dynamic flow resistances for 4 cases with straight holes (a) and 4 cases with tapered holes (b). CFD results (solid) are compared with results from Eq. 23 (dashed).

FIG. 11. (Color online) For a straight case (#2 in Table 2) the velocity magnitude (m/s) is shown in the upper row and the corresponding shear rate (1/s) is shown in the lower row. The times from left to right are at 30, 50, 70, and 90 μs.

FIG. 12. (Color online) Resistance (a) and reactance (b) plots for a straight case (#2 from Table 2). Corresponding formula results using Eq. 22, Eq. 1 (Maa) and Eq. 6 (Guo) with α=2 and α=4 are shown as well.

FIG. 13. (Color online) For the tapered case (#5 in Table 2) the velocity field (m/s) is shown in the upper row and the corresponding shear rate (1/s) is shown in the lower row. The times from left to right are at 30, 50, 70, and 90 μs.

FIG. 14. (Color online) Resistance (a) and reactance (b) plots for straight and tapered cases (#2 and #5 from Table). Corresponding formula results using Eq. 23 are shown as well. Only a slight difference between forward and reverse flow can be seen in the resistance plot.

FIG. 15. (Color online) Dynamic flow resistances for cases with equal static flow resistance, from Table 2. Sketches of the eight hole designs, all on equal scales, are shown so the length and diameter of the holes can better be compared; additionally, the horizontal extent of the film (shown shaded) gives an indication of the hole density.

FIG. 16. (Color online) Absorption coefficients for cases with equal static flow resistance, from Table 2, and a rigidly terminated air space of 25 mm. Graph (a) shows results using the impedance from the CFD calculations, and graph (b) shows the results using the impedance from Eq. 23.